



# A physical model of Direct Methanol Fuel Cell anode impedance



M. Zago\*, A. Casalegno

Politecnico di Milano, Department of Energy, Via Lambruschini 4, 20156 Milano, Italy

## HIGHLIGHTS

- We developed and validated a physically based impedance model of DMFC anode.
- Liquid convection through gas diffusion layer is an intermittent phenomenon.
- Mass transport losses through gas diffusion layer are relevant even at low current densities.
- Oscillation of membrane cross-over fluxes influences low-medium frequency region.

## ARTICLE INFO

### Article history:

Received 28 March 2013  
Received in revised form  
3 September 2013  
Accepted 13 October 2013  
Available online 23 October 2013

### Keywords:

Anode  
Direct methanol fuel cell  
Electrochemical impedance spectroscopy  
Model

## ABSTRACT

In the present work a physically based model of direct methanol fuel cell anode impedance has been developed and validated at different operating current densities. The proposed model includes the two-phase mass transport of both methanol and water through diffusion and catalyst layers and the methanol oxidation reaction involving CO adsorbed intermediate. Model simulations are in good quantitative agreement with experimental observations and permit to evaluate the origin of anode impedance features. Model results confirm that the high frequency 45° linear branch is caused by proton transport limitations within the catalyst layer and that the low frequency inductive behavior is due to surface coverage by CO reaction intermediate. Moreover model predictions elucidate the contribution to the impedance of mass transport phenomena through diffusion layer, that is relevant even at low current density and increases along the channel length. In particular liquid convective fluxes are considered as a process of pressure buildup and breakthrough at diffusion layer intersecting fibers, resulting in a discontinuous phenomenon. By means of this intermittent description it is possible to correctly reproduce mass transport limitations through diffusion layers, that manifest themselves as a second arch superimposed to the first one, peculiar of kinetic losses.

© 2013 Elsevier B.V. All rights reserved.

## 1. Introduction

The Electrochemical Impedance Spectroscopy (EIS) is a powerful in-situ measurement technique that permits to evaluate the kinetic and transport phenomena of an electrochemical system [1,2]. It consists in perturbing the fuel cell operation with a small AC current signal over a wide range of frequencies and in measuring the voltage response. The module and the phase shift between voltage response and current perturbation are due to the electrical impedance of the fuel cell and provide useful information on the entity of internal fuel cell losses.

Despite the potentialities of this measurement technique the interpretation of experimental observations is very complicated

and modeling plays a fundamental role in the analysis of experimental data. Until now the interpretation has mostly been carried out by means of equivalent circuit method (ECM) [3–6]. Even though simple and fast, this method is not reliable, since the equivalent circuit is not unique; moreover ECM provides only few useful qualitative information.

M. Orazem [7] proposed an innovative approach for a quantitative interpretation of EIS measurements: the developed methodology consists in expressing the equivalent circuit element as a function of the physical parameters of the system. In Ref. [8] this method was used for the interpretation of cathode impedance of a polymer electrolyte membrane fuel cell (PEMFC), but in principle it could be applied to any electrochemical system, including direct methanol fuel cell (DMFC). However the results still depend on the considered equivalent electric circuit. A similar methodology has been adopted by T.S. Zhao et al. [9] to investigate the simultaneous oxygen reduction and methanol oxidation at the cathode of a DMFC.

\* Corresponding author.

E-mail addresses: [matteo.zago@mail.polimi.it](mailto:matteo.zago@mail.polimi.it), [matteo1.zago@polimi.it](mailto:matteo1.zago@polimi.it), [zago.matte@gmail.com](mailto:zago.matte@gmail.com) (M. Zago).

An alternative approach is represented by physically based EIS models, that in the last years attracted increasing scientific interest [10–19]. The development and experimental validation of this type of models are very complicated, but the results are not related to the choice of a suitable equivalent electric circuit and model predictions permit to investigate the origin of different impedance features.

In the literature many works regarding both solid oxide fuel cells (SOFCs) [10–12] and PEMFCs [13,14] technology can be found. Bessler et al. carried out an extensive physically based model activity on SOFC [15–17]: the flexibility and modularity of the developed models, including detailed elementary kinetic electrochemistry and diffusion processes, allowed the assignment of the origin of SOFC impedance features with high accuracy. Springer et al. [18] developed one of the first numerical models for PEMFC cathode impedance: the first impedance loop was attributed to the effective charge-transfer resistance and double-layer charging, while the second one was related to the mass-transport limitation in the gas phase. Guo and White [19] presented a PEMFC cathode impedance model consisting of many flooded spherical agglomerate particles, permitting a more detailed comprehension on impedance behavior.

In DMFCs the anode catalyst layer (CL) internal losses are not negligible, as in PEMFC technology; moreover the mass transport phenomena at anode side are very complex, due to the two-phase and multi-component nature of the flows. Thus the interpretation of impedance behavior is even more complicated than in PEFC and SOFC technology, in fact in the literature only few modeling analyses can be found [20–24], generally concerning the cathode.

Kulikovsky reported a clear and detailed explanation of the mathematical development of DMFC cathode impedance model [20,21], analyzing the effects of physical phenomena on the shape of cathode impedance spectrum. However the models are not integrated along channel length and no attempts to fit experimental data have been done. Sundmacher et al. presented a detailed analysis of the methanol oxidation kinetics on a DMFC anode in a cyclone flow cell [23], but the homogeneous concentration distribution over the membrane electrode assemblies (MEA) does not permit to investigate mass transport limitations. Therefore in the literature limited effort has been dedicated to develop a whole DMFC anode impedance model and a detailed comprehension of the physicochemical phenomena regulating anode operation is required to further optimize components, operation strategies and lifetime.

This work proposes a complete and validated physical model of DMFC anode impedance, increasing the understanding of anode operation and providing a quantitative interpretation of the experimental measurements. The work is organized as follows. In Section 2 the experimental measurement of DMFC anode impedance is reported, subsequently, in Section 3, the model development is described. Then, in Section 4, the model results and the origin of different impedance features are illustrated and finally some conclusions are given in Section 5.

## 2. Experimental

### 2.1. Cell hardware

The experimental measurements were conducted using the same fuel cell, as well as equipment, which has already been characterized in terms of anode polarization, performance, methanol cross-over and water transport in previous publications by the authors [25–27].

The MEA was purchased already assembled by balticFuelCells GmbH with an active area of  $22.1 \text{ cm}^2$ , consisting of Pt–Ru anode

( $4 \text{ mg cm}^{-2}$ , Pt:Ru = 2), a Nafion® 117 membrane and Pt cathode ( $4 \text{ mg cm}^{-2}$ ). Anode diffusion layer presents gas diffusion layer (GDL) without micro porous layer (MPL), while the cathode one has got MPL: for this reason this MEA is named MEA GM, as in previous publication [27]. The fuel cell is thermostated at 333 K, the anode is supplied with a 3.25wt.% aqueous solution of methanol at  $1 \text{ g min}^{-1}$  flow rate, while the cathode operates with a hydrogen flow rate (see paragraph 2.2) of  $2.14 \cdot 10^{-4} \text{ g min}^{-1}$ .

### 2.2. Electrochemical measurements

In hydrogen–air fuel cells contributions of the anode are usually negligible due to fast kinetics of hydrogen oxidation reaction and a standard practice consists in neglecting anode impedance [18]. In DMFC the slow methanol electro-oxidation does not permit to clearly distinguish anode and cathode contributions by measuring the full fuel cell impedances. However it is possible to eliminate contributions of the cathode in a half-cell DMFC by feeding the cathode with hydrogen, so that protons are reduced and hydrogen is evolved [28–31]. In this configuration the cathode works as a dynamic hydrogen electrode (DHE) and it is suitable as a reference and counter electrode for DMFC anode impedance measurements.

The anode spectra were recorded with an Autolab PGSTAT 30® provided with a frequency response analysis module. The impedances are measured under galvanostatic control and the amplitude of the sinusoidal current signal is adjusted so that the potential amplitude does not exceed 10 mV. The frequency is included between 10 kHz and 50 mHz with a logarithmic distribution. The obtained experimental values are processed by a retrospective use of Kramers–Kronig transforms [1,32] in order to verify the validity of the measurements. The impedance values that do not satisfy such relations are not considered meaningful. Fig. 1 reports two

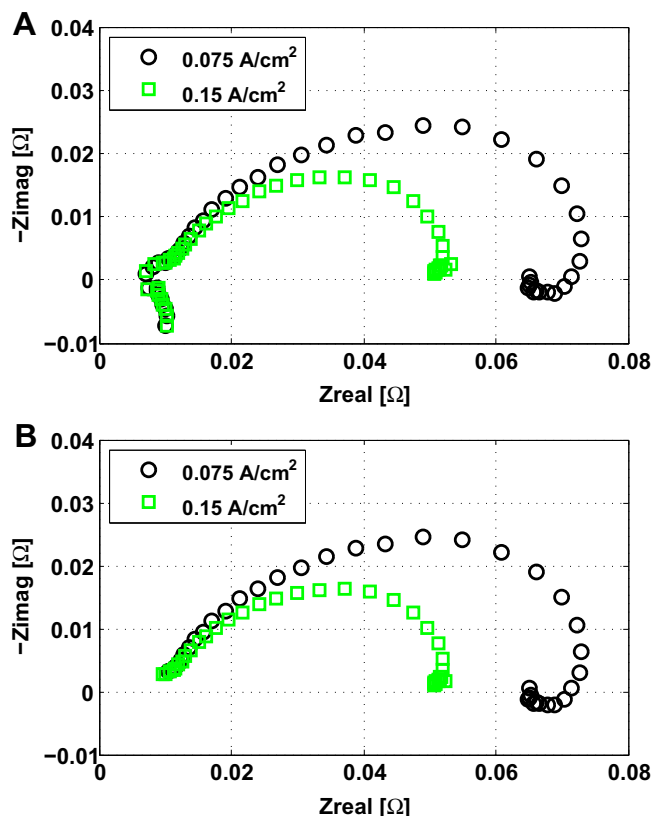


Fig. 1. Anode Nyquist plots at different current densities: a) raw data; b) after the use of Kramers–Kronig relations.

anode spectra measured at  $0.075 \text{ A cm}^{-2}$  and  $0.15 \text{ A cm}^{-2}$  before and after the use of Kramers–Kronig relations. It is evident that the high frequencies region is not consistent with these relations, because of instrument limitation, and therefore the corresponding measurement points are eliminated from the spectra.

The anode impedances of Fig. 1 are an elongated semicircle: this is partially due to proton transport losses in the CL, that manifest themselves as almost  $45^\circ$  linear branch at high frequencies. By varying the operating current density, two relevant differences are appreciable in the low frequency region. At  $0.075 \text{ A cm}^{-2}$  an inductive behavior is evident: this could be due to the catalyst surface coverage by adsorbed reaction intermediates. At  $0.15 \text{ A cm}^{-2}$  the inductive behavior is no longer present, but mass transport limitations seem to appear in the low frequencies region. This impedance feature is coherent with the increased mass transport fluxes through the GDL.

However in the literature the interpretation of DMFC anode impedance is not fully consolidated [33] and in the next sections a physically based impedance model of DMFC anode is presented and discussed, in order to provide a more solid and quantitative interpretation of experimental observations.

### 3. Model development

In this paragraph a previously developed 1D+1D DMFC model [27,34] has been firstly integrated with a detailed description of mass transport phenomena through anode GDL and a CL with a finite thickness. Subsequently, considering the same mathematical approach presented in Refs. [20,21], a DMFC anode impedance model has been developed.

#### 3.1. Diffusion layer model

In the 1D + 1D DMFC model presented in Refs. [27,34], due to the high availability of water at the anode, the phenomena governing water transport through anode GDL are omitted; the water transport through the MEA is assumed to be regulated by water transport through the membrane and cathode diffusion layer. Moreover in the original model the methanol flux through the anode GDL is governed by gas and liquid diffusion, assuming that liquid saturation is constant across the diffusion layer thickness (Eq. (18) in Ref. [34]).

In the developed model the following improvements have been introduced:

- the water is transported through the anode GDL by liquid convection, Fig. 2: however the water transport through the MEA is

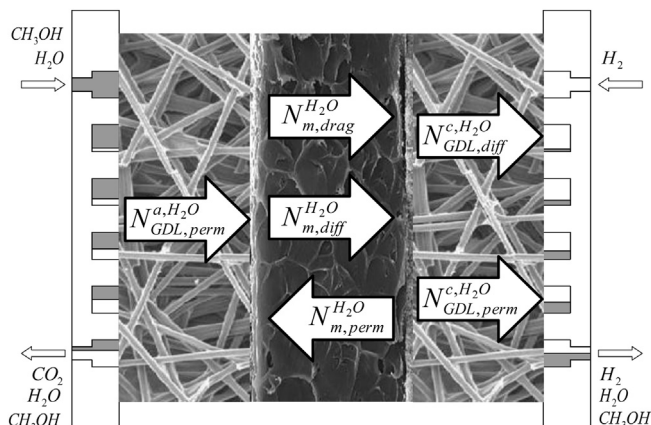


Fig. 2. Water fluxes through the DMFC during anode polarization.

still regulated by water transport through the membrane and cathode diffusion layer, coherently with the previously proposed interpretations of water management [27];

- the contribution of methanol liquid convection through anode GDL is considered;
- liquid saturation is no longer constant across the anode diffusion layer thickness due to the liquid convective fluxes.

The equations that fully describe mass transport phenomena through anode GDL are the following:

$$-D_{\text{GDL,CH}_3\text{OH}}^L \cdot s_{\text{GDL}} \cdot \frac{\partial C_{\text{CH}_3\text{OH}}^{\text{GDL,L}}}{\partial x} - D_{\text{GDL,CH}_3\text{OH}}^G \cdot (1 - s_{\text{GDL}}) \cdot \frac{\partial C_{\text{CH}_3\text{OH}}^{\text{GDL,G}}}{\partial x} = N_{\text{GDL}}^{\text{CH}_3\text{OH}} - N_{\text{GDL}}^{\text{H}_2\text{O}} \cdot \frac{C_{\text{CH}_3\text{OH}}^{\text{GDL,L}}}{C_{\text{H}_2\text{O}}^{\text{GDL,L}}} \quad (1)$$

$$\frac{\partial s_{\text{GDL}}}{\partial x} = \frac{1}{s_{\text{GDL}}^3 \cdot (1.417 - 4.24 \cdot s_{\text{GDL}} + 3.789 \cdot s_{\text{GDL}}^2)} \times \frac{M_{\text{H}_2\text{O}} \cdot \nu_{\text{H}_2\text{O}}}{\sigma_{\text{H}_2\text{O}} \cdot \cos \theta_c \cdot (\varepsilon_{\text{GDL}} \cdot K_{\text{GDL}})^{0.5}} \cdot N_{\text{GDL}}^{\text{H}_2\text{O}} \quad (2)$$

$$\frac{\partial N_{\text{GDL}}^{\text{CH}_3\text{OH}}}{\partial x} = -\varepsilon_{\text{GDL}} \cdot s_{\text{GDL}} \cdot \frac{\partial C_{\text{CH}_3\text{OH}}^{\text{GDL,L}}}{\partial t} - \varepsilon_{\text{GDL}} \cdot (1 - s_{\text{GDL}}) \cdot \frac{\partial C_{\text{CH}_3\text{OH}}^{\text{GDL,G}}}{\partial t} \quad (3)$$

$$\frac{\partial N_{\text{GDL}}^{\text{H}_2\text{O}}}{\partial x} = -\varepsilon_{\text{GDL}} \cdot s_{\text{GDL}} \cdot \frac{\partial C_{\text{H}_2\text{O}}^{\text{GDL,L}}}{\partial t} - \varepsilon_{\text{GDL}} \cdot (1 - s_{\text{GDL}}) \cdot \frac{\partial C_{\text{H}_2\text{O}}^{\text{GDL,G}}}{\partial t} \quad (4)$$

Eq. (1) is the Fick's law of diffusion for two-phase methanol, in which the second term in the right hand side of the equation is the contribution of methanol liquid convection. As proposed in Refs. [34], the methanol concentrations in gas and liquid phases are considered in equilibrium, described by Henry's law:

$$C_{\text{CH}_3\text{OH}}^{\text{GDL,L}} = K_{\text{H,CH}_3\text{OH}} \cdot C_{\text{CH}_3\text{OH}}^{\text{GDL,G}} \cdot R \cdot T \quad (5)$$

Eq. (2) is the governing equation of water transport, that is described by the Leverett function [35]. Eqs. (3) and (4) express the mass balance of methanol and water, respectively; the liquid phase accumulation term is proportional to the liquid saturation, while the gas phase one is proportional to the void fraction.

Particular attention has been given to the understanding of the mechanisms regulating liquid convective fluxes. In fact the GDL is not assumed to be always flooded with fully liquid pathways, as widely accepted in the literature [35,36]. Recent studies on liquid convection through GDLs [37,38] showed that liquid paths are intermittent and breakthrough locations change with time. These flow visualizations [37,38] suggest that the liquid transport within the GDL is a process of capillary pressure buildup and breakthrough at the interface of GDL intersecting fibers, Fig. 3 a. When the liquid pressure exceeds the breakthrough value, the liquid expands rapidly through this interface until the fluid contacts the next fiber intersections interface, Fig. 3b. Then the process of pressure buildup and breakthrough begins again until the fluid reaches the GDL-CL interface, Fig. 3c. At this interface, when the capillary pressure exceeds the threshold value, the liquid is quickly removed from GDL pores, that become empty, Fig. 3d. The dynamic of liquid emergence and detachment from GDL surface is very fast, in the order of few milliseconds, and it is enhanced by GDL hydrophobicity [39,40].

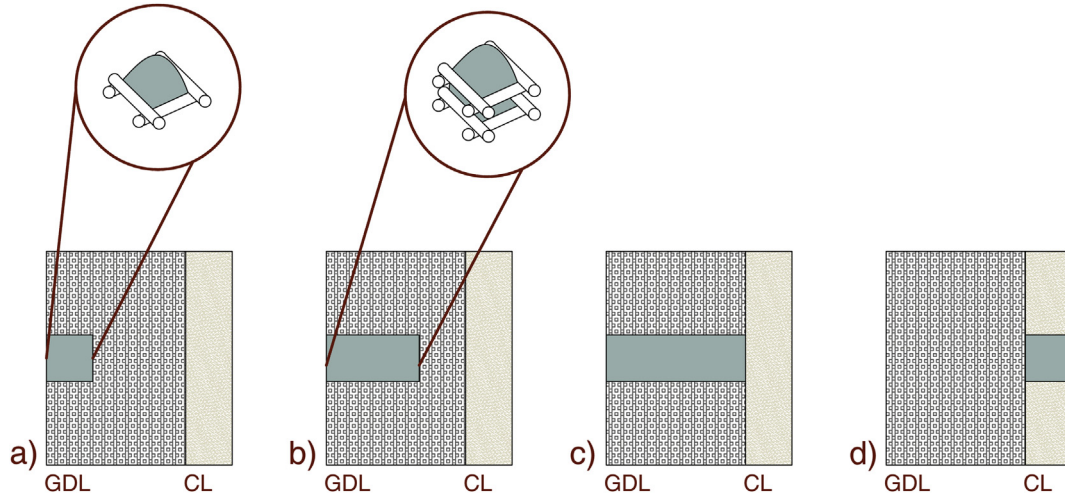
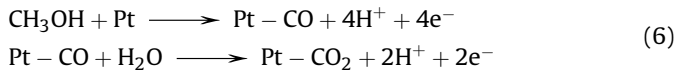


Fig. 3. Schematic illustration of intermittent liquid convection.

The proposed description of intermittent liquid convective flux implies that the effect of liquid accumulation terms in the GDL, Eqs. (3) and (4), is only present meanwhile liquid flux to the CL effectively occurs,<sup>1</sup> or rather for frequencies higher than tens of Hertz. In this work a threshold value of 75 Hz is assumed.

### 3.2. Catalyst layer model

In the original 1D+1D DMFC model [27,34] the CL is assumed to be monodimensional in the direction of channel length. In this work a CL with a finite thickness is introduced in the model in order to take into account proton transport limitations. Moreover, coherently with the presence of low frequency inductive loop (Fig. 1), a reaction mechanism involving intermediate adsorbates is considered. In particular the following two-steps reaction mechanisms with a single adsorbed intermediate is proposed [29,41,42]:



In the first reaction step the adsorbed intermediate CO is formed in the process of methanol dehydrogenation, while in the second reaction step adsorbed CO undergoes further oxidation to CO<sub>2</sub> in a process involving the transfer of two protons and two electrons.

The system that fully describes the CL behavior is the following:

$$\frac{\partial i}{\partial x} = i_1 + i_2 \quad (7)$$

$$-\bar{D}_{\text{t,CH}_3\text{OH}} \cdot \frac{\partial^2 \bar{C}_{\text{CH}_3\text{OH}}^{\text{t}}}{\partial x^2} = -\frac{1}{4 \cdot F} \cdot i_1 - \varepsilon_{\text{t}} \cdot \frac{\partial \bar{C}_{\text{CH}_3\text{OH}}^{\text{t}}}{\partial t} \quad (8)$$

$$-\bar{D}_{\text{t,H}_2\text{O}} \cdot \frac{\partial^2 \bar{C}_{\text{H}_2\text{O}}^{\text{t}}}{\partial x^2} = -\frac{1}{2 \cdot F} \cdot i_2 - \varepsilon_{\text{t}} \cdot \frac{\partial \bar{C}_{\text{H}_2\text{O}}^{\text{t}}}{\partial t} \quad (9)$$

$$\frac{\partial \eta}{\partial x} = \frac{i}{\sigma_{\text{t}}} \quad (10)$$

<sup>1</sup> Note that when no liquid flux to the CL occurs, this intermittent description excludes the effect, but not the presence, of liquid accumulations in the GDL.

$$I_{\text{Pt}} \cdot \frac{\partial \gamma_{\text{CO}}}{\partial t} = \frac{1}{4 \cdot F} \cdot i_1 - \frac{1}{2 \cdot F} \cdot i_2 \quad (11)$$

where:

$$i_1 = i_{*1} \cdot \frac{\bar{C}_{\text{CH}_3\text{OH}}^{\text{t}}}{\bar{C}_{\text{ref},1}} \cdot (1 - \gamma_{\text{CO}}) \cdot \exp(\eta/b_1) \quad (12)$$

$$i_2 = i_{*2} \cdot \frac{\bar{C}_{\text{H}_2\text{O}}^{\text{t}}}{\bar{C}_{\text{ref},2}} \cdot \gamma_{\text{CO}} \cdot \exp(\eta/b_2) \quad (13)$$

Eq. (7) describes charge conservation in the CL, while Eqs. (8) and (9) express the mass balance of methanol and water, respectively. Due to the strong uncertainties related to the two-phase mass transport phenomena in the CL [43], considering for example the mixture phase transition and the evolution of CO<sub>2</sub> bubbles, average concentrations and diffusivities are considered for simplicity. In particular, the average diffusivities of methanol and water are assumed equal to each other and proportional to the average diffusivity of the GDL:

$$\bar{D}_{\text{t,CH}_3\text{OH}} = \bar{D}_{\text{t,H}_2\text{O}} = \frac{N_{\text{GDL}}^{\text{CH}_3\text{OH}} \cdot l_{\text{GDL}}}{\Delta C^{\text{GDL,L}} \cdot \bar{s}_{\text{GDL}} + \Delta C^{\text{GDL,G}} \cdot (1 - \bar{s}_{\text{GDL}})} \cdot CF \quad (14)$$

CF is a correction factor, that takes into account the different porosity and void fraction of the CL.

Eq. (10) is the Ohm's law relating the proton current density to the gradient of overpotential; it is necessary to take into account the proton transport limitations in the impedance spectrum. Eq. (11) describes the variation of the surface coverage by the CO adsorbed intermediate: the first reaction step produces CO coverage, while the second reaction step consumes CO coverage.

### 3.3. DMFC anode polarization model

During anode polarization cathode is considered a reference electrode, in particular a dynamic hydrogen electrode [44], whose potential is nearly constant and negligible in comparison to anode. Therefore in the DMFC anode polarization model the cathode overpotential is neglected and the voltage variations are mainly attributable to anode and membrane overpotentials, as described



in Ref. [45]. The Eq. (29) in Ref. [34] is thus replaced by the following:

$$V_{\text{cell}} = \eta^a + \eta^{\text{ohm}} \quad (15)$$

Regarding the continuity equations at cathode side, the following modifications have been introduced:

- air is replaced by hydrogen and therefore Eqs. (12) and (15) in Ref. [34] are substituted with:

$$\frac{h^c}{2} \cdot \frac{\partial(\nu^c \cdot C_{\text{H}_2}^c)}{\partial x} = \frac{i}{2 \cdot F} \quad (16)$$

- $\text{CO}_2$ , Eq. (13) in Refs. [34], is removed because the methanol cross-over flux is no longer oxidized;
- water production in the cathode CL is not considered because of the hydrogen feeding and Eq. (14) in Ref. [34] becomes:

$$\frac{h^c}{2} \cdot \frac{\partial(\nu^c \cdot \bar{C}_{\text{H}_2\text{O}}^c)}{\partial x} = N_{\text{m,cross}}^{\text{H}_2\text{O}} \quad (17)$$

Indeed the systems characterizing GDL, Eqs. (1)–(4), and CL behavior, Eqs. 7–11, have been introduced in the above described DMFC anode polarization model. The GDL equations are solved applying the appropriate boundary conditions regarding methanol concentration and saturation at the channel-GDL interface,  $s_{\text{ch-GDL}}$ . The complicated two-phase hydrodynamics in the channel makes the liquid saturation at this interface difficult to be determined theoretically. In the literature, the most of the works [46,47] suppose its value: in Ref. [46] it is equal to 0.8, while in Ref. [47] it is equal 0.65, despite the lower hydrophobicity of the considered diffusion media. Moreover, the above cited works [46,47] propose a 1D model along the thickness of the DMFC and no attempts to calculate  $s_{\text{ch-GDL}}$  profile along channel length have been done. In Refs. [48], in which a complete DMFC model is presented, the saturation at channel-GDL interface is assumed equal to the channel one: however this assumption is not coherent with the different hydrophilic–hydrophobic properties between the channel and the diffusion media. In Refs. [49], instead, an empirical approach is taken: the boundary condition regarding  $s_{\text{ch-GDL}}$  profile along channel length is expressed as a function of the current density. According to Ref. [49], also in this work an empirical approach is adopted. However the saturation is not assumed directly proportional to the current density, but the following dependence on saturation in the channel is proposed:

$$s_{\text{ch-GDL}} = S_1 \cdot s_{\text{ch}}^2 + S_3 \quad (18)$$

where  $s_{\text{ch}}$  is the saturation in the channel and the parameters  $S_1$ ,  $S_2$  and  $S_3$  are calibrated over experimental data. Subsequently, as widely accepted in the literature [46,50], the liquid saturation at the GDL-CL interface in the electrode can be calculated by assuming that the capillary pressure remains uniform across the interface:

$$p_{\text{c}}|_{\text{GDL-el}^-} = p_{\text{c}}|_{\text{GDL-el}^+} \quad (19)$$

According to Ref. [35], the capillary pressure can be expressed as:

$$p_{\text{c}} = \sigma_{\text{H}_2\text{O}} \cdot \cos\theta_{\text{c}} \cdot (\varepsilon/K)^{0.5} \cdot J(s) \quad (20)$$

where  $J(s)$  is the Leverett function and for a hydrophobic medium is given by the following relation:

$$J(s) = 1.417 \cdot s - 2.120 \cdot s^2 + 1.263 \cdot s^3 \quad (21)$$

The system describing CL behavior is subject to the following boundary conditions:

$$i|_{\text{GDL-el}} = 0 \quad (22)$$

$$i|_{\text{el-m}} = i_{\text{cell}} \quad (23)$$

$$-\bar{D}_{\text{t,CH}_3\text{OH}} \cdot \frac{\partial \bar{C}_{\text{CH}_3\text{OH}}^{\text{t}}}{\partial x} \Big|_{\text{GDL-el}} = N_{\text{GDL}}^{\text{CH}_3\text{OH}} \quad (24)$$

$$-\bar{D}_{\text{t,CH}_3\text{OH}} \cdot \frac{\partial \bar{C}_{\text{H}_2\text{O}}^{\text{t}}}{\partial x} \Big|_{\text{GDL-el}} = N_{\text{GDL}}^{\text{H}_2\text{O}} \quad (25)$$

$$\bar{C}_{\text{CH}_3\text{OH}}^{\text{t}} \Big|_{\text{GDL-el}} = s_{\text{el}} \cdot C_{\text{CH}_3\text{OH}}^{\text{L}} \Big|_{\text{GDL-el}} + (1 - s_{\text{el}}) \cdot C_{\text{CH}_3\text{OH}}^{\text{G}} \Big|_{\text{GDL-el}} \quad (26)$$

$$\bar{C}_{\text{H}_2\text{O}}^{\text{t}} \Big|_{\text{GDL-el}} = s_{\text{el}} \cdot C_{\text{H}_2\text{O}}^{\text{L}} \Big|_{\text{GDL-el}} + (1 - s_{\text{el}}) \cdot C_{\text{H}_2\text{O}}^{\text{sat}} \quad (27)$$

This is a two-point boundary value problem and the built in BVP function of MATLAB® environment has been used for the numerical resolution of the system of Eqs. 7–11.

By solving the entire DMFC anode polarization model it is therefore possible to obtain the steady-state profiles along channel length and both GDL and CL thickness of all the quantities necessary for the development of the physically based DMFC anode impedance model, reported in the next paragraph.

### 3.4. DMFC anode impedance model

After obtaining the stationary solution, the transient perturbation solution of the DMFC anode can be obtained in the following way. Eqs. (2) and (7) are linearized about a steady-state value and subsequently each of the variables  $z_i$  of Eqs. (1)–(4) and (7)–(11) are perturbed about a steady-state value with a sufficiently low sinusoidal disturbance:

$$z_i(t) = z_i^0 + \text{Re}\{\Delta z_i \cdot \exp(j \cdot \omega \cdot t)\} \quad (28)$$

Neglecting the terms with products of the disturbances and subtracting the steady-state equations, it is possible to obtain a system of linear equations for the complex perturbation amplitudes  $\Delta z_i$  in the frequency domain, as reported in Refs. [20,21]. In particular the GDL equations (1)–(4) become:

$$\begin{aligned} \frac{\partial \Delta C_{\text{CH}_3\text{OH}}^{\text{GDL,L}}}{\partial x} & \cdot \left( D_{\text{GDL,CH}_3\text{OH}}^{\text{L}} \cdot s_{\text{GDL}}^0 + \frac{D_{\text{GDL,CH}_3\text{OH}}^{\text{G}}}{K_{\text{H,CH}_3\text{OH}} \cdot R \cdot T} \cdot (1 - s_{\text{GDL}}^0) \right) \\ & = -\Delta N_{\text{GDL}}^{\text{CH}_3\text{OH}} + \Delta N_{\text{GDL}}^{\text{H}_2\text{O}} \cdot \frac{C_{\text{CH}_3\text{OH}}^{\text{GDL,L,0}}}{C_{\text{H}_2\text{O}}^{\text{GDL,L,0}}} + N_{\text{GDL}}^{\text{H}_2\text{O},0} \cdot \frac{\Delta C_{\text{CH}_3\text{OH}}^{\text{GDL,L}}}{C_{\text{H}_2\text{O}}^{\text{GDL,L,0}}} \\ & \quad - \Delta s_{\text{GDL}} \cdot \left( D_{\text{GDL,CH}_3\text{OH}}^{\text{L}} - \frac{D_{\text{GDL,CH}_3\text{OH}}^{\text{G}}}{K_{\text{H,CH}_3\text{OH}} \cdot R \cdot T} \right) \cdot \frac{\partial C_{\text{CH}_3\text{OH}}^{\text{GDL,L}}}{\partial x} \Big|_0 \end{aligned} \quad (29)$$

$$\frac{\partial \Delta s_{\text{GDL}}}{\partial x} = \frac{M_{\text{H}_2\text{O}} \cdot \nu_{\text{H}_2\text{O}}}{\sigma_{\text{H}_2\text{O}} \cdot \cos \theta_c \cdot (\varepsilon_{\text{GDL}} \cdot K_{\text{GDL}})^{0.5}} \cdot \left( \frac{N_{\text{GDL}}^{\text{H}_2\text{O},0}}{f'(s_{\text{GDL}}^0)} \cdot \Delta s_{\text{GDL}} + \frac{1}{f(s_{\text{GDL}}^0)} \cdot \Delta N_{\text{GDL}}^{\text{H}_2\text{O}} \right) \quad (30)$$

$$\frac{\partial \Delta N_{\text{GDL}}^{\text{CH}_3\text{OH}}}{\partial x} = -j \cdot \omega \cdot \varepsilon_{\text{GDL}} \cdot \left( \Delta s_{\text{GDL}} \cdot C_{\text{CH}_3\text{OH}}^{\text{GDL,L},0} + \Delta C_{\text{CH}_3\text{OH}}^{\text{GDL,L}} \cdot s_{\text{GDL}}^0 \right) + j \cdot \omega \cdot \varepsilon_{\text{GDL}} \cdot \left( \frac{\Delta s_{\text{GDL}} \cdot C_{\text{CH}_3\text{OH}}^{\text{GDL,L},0} - \Delta C_{\text{CH}_3\text{OH}}^{\text{GDL,L}} + \Delta C_{\text{CH}_3\text{OH}}^{\text{GDL,L}} \cdot s_{\text{GDL}}^0}{K_{\text{H},\text{CH}_3\text{OH}} \cdot R \cdot T} \right) \quad (31)$$

$$\frac{\partial \Delta N_{\text{GDL}}^{\text{H}_2\text{O}}}{\partial x} = -j \cdot \omega \cdot \varepsilon_{\text{GDL}} \cdot \left( \Delta s_{\text{GDL}} \cdot C_{\text{H}_2\text{O}}^{\text{GDL,L},0} - \Delta s_{\text{GDL}} \cdot C_{\text{H}_2\text{O}}^{\text{sat}} \right) \quad (32)$$

where:

$$f(s_{\text{GDL}}) = s_{\text{GDL}}^3 \cdot (1.417 - 4.24 \cdot s_{\text{GDL}} + 3.789 \cdot s_{\text{GDL}}^2) \quad (33)$$

While the CL equations 7–11 take the following form:

$$\frac{\partial \Delta i}{\partial x} = \Delta i_1 + \Delta i_2 + j \cdot \omega \cdot C_{\text{dl}} \cdot \Delta \eta \quad (34)$$

$$\frac{\partial \Delta N_{\text{t}}^{\text{CH}_3\text{OH}}}{\partial x} = \frac{\Delta i_1}{4 \cdot F} - j \cdot \omega \cdot \varepsilon_{\text{t}} \cdot \Delta \bar{C}_{\text{CH}_3\text{OH}}^{\text{t}} \quad (35)$$

$$\frac{\partial \Delta N_{\text{t}}^{\text{H}_2\text{O}}}{\partial x} = \frac{\Delta i_2}{2 \cdot F} - j \cdot \omega \cdot \varepsilon_{\text{t}} \cdot \Delta \bar{C}_{\text{H}_2\text{O}}^{\text{t}} \quad (36)$$

$$-\bar{D}_{\text{t},\text{CH}_3\text{OH}} \cdot \frac{\partial \Delta \bar{C}_{\text{CH}_3\text{OH}}^{\text{t}}}{\partial x} = \Delta N_{\text{t}}^{\text{CH}_3\text{OH}} \quad (37)$$

$$-\bar{D}_{\text{t},\text{H}_2\text{O}} \cdot \frac{\partial \Delta \bar{C}_{\text{H}_2\text{O}}^{\text{t}}}{\partial x} = \Delta N_{\text{t}}^{\text{H}_2\text{O}} \quad (38)$$

$$\frac{\partial \Delta \eta}{\partial x} = \frac{\Delta i}{\sigma_{\text{t}}} \quad (39)$$

$$j \cdot \omega \cdot \Delta \gamma_{\text{CO}} \cdot \Gamma_{\text{Pt}} = \frac{\Delta i_1}{4 \cdot F} - \frac{\Delta i_2}{2 \cdot F} \quad (40)$$

where  $\Delta i_1$  and  $\Delta i_2$  are equal to:

$$\Delta i_1 = \left. \frac{\partial i_1}{\partial \eta} \right|_0 \cdot \Delta \eta + \left. \frac{\partial i_1}{\partial \bar{C}_{\text{CH}_3\text{OH}}^{\text{t}}} \right|_0 \cdot \Delta \bar{C}_{\text{CH}_3\text{OH}}^{\text{t}} + \left. \frac{\partial i_1}{\partial \gamma_{\text{CO}}} \right|_0 \cdot \Delta \gamma_{\text{CO}} \quad (41)$$

$$\Delta i_2 = \left. \frac{\partial i_2}{\partial \eta} \right|_0 \cdot \Delta \eta + \left. \frac{\partial i_2}{\partial \bar{C}_{\text{H}_2\text{O}}^{\text{t}}} \right|_0 \cdot \Delta \bar{C}_{\text{H}_2\text{O}}^{\text{t}} + \left. \frac{\partial i_2}{\partial \gamma_{\text{CO}}} \right|_0 \cdot \Delta \gamma_{\text{CO}} \quad (42)$$

The boundary conditions to Eq. 29–32 and Eq. 34–40 are as following:

$$\Delta \eta|_{\text{GDL-el}} = \eta_{\text{EIS}} \quad (43)$$

$$\Delta i|_{\text{GDL-el}} = 0 \quad (44)$$

$$\Delta C_{\text{CH}_3\text{OH}}|_{\text{ch-GDL}} = 0 \quad \Delta C_{\text{H}_2\text{O}}|_{\text{ch-GDL}} = 0 \quad (45)$$

$$\Delta N_{\text{CH}_3\text{OH}}|_{\text{el-m}} = \Delta N_{\text{m,drag}}^{\text{CH}_3\text{OH}} \quad \Delta N_{\text{H}_2\text{O}}|_{\text{el-m}} = \Delta N_{\text{m,drag}}^{\text{H}_2\text{O}} \quad (46)$$

Eq. (43) establishes a small amplitude perturbation at GDL-CL interface. As demonstrated in Refs. [20], the system of Eq. 29–32 and Eq. 34–40 is linear and homogenous and the impedance does not depend on the amplitude of this boundary condition. Eq. (44) means null proton current at the GDL-CL interface. Eq. (45) expresses zero disturbance of methanol and water concentration at channel-GDL interface, respectively. This implies that the concentration in the channel remains unperturbed by the change in overpotential: considering the high liquid accumulation in the channel, that is present for all the perturbation frequencies, this is a reasonable assumption. Since the membrane is permeable to both methanol and water, the oscillation of the corresponding flux at the membrane interface cannot be assumed equal to zero. As reported in Refs. [27], water cross-over flux is regulated by electro-osmotic drag and liquid diffusion and convection, while the methanol cross-over flux is only governed by electro-osmotic drag and liquid diffusion. The contributions of liquid diffusion and convection are influenced by the corresponding concentration and pressure at the cathode side, that during dynamic operation are difficult to be determined with a suitable uncertainty. Considering also the considerable accumulation in the membrane, Eq. (46) imposes that the disturbance of methanol and water flux is equal only to the oscillation of drag component.

Finally the impedance of the anode can be numerically calculated as the ration between the oscillating voltage and current density at CL-membrane interface:

$$Z = \frac{\Delta \eta}{\Delta i}|_{\text{el-m}} \quad (47)$$

The system of Eq. 29–32 and Eq. 34–40, along with the boundary conditions Eq. 43–46, is solved in MATLAB® environment. In particular the FSOLVE function solves the CL equations, Eq. 34–40, by iteratively changing the value of the oscillatory fluxes at electrode inlet till the boundary conditions, Eq. (46), are satisfied. At the same time these fluxes are imposed, together with Eq. (45), as boundary conditions in a BVP function, that solves the GDL equations, Eq. 29–32. In this way all the boundary conditions reported in Eq. 43–46 are simultaneously satisfied and the iterations are performed by means of an optimized built in function, increasing the numerical stability of the problem.

Furthermore, considering all the steady-state profiles obtained by the DMFC anode polarization model, it is possible to calculate the local value of DMFC impedance along channel length. Thus the total impedance is equal to the parallel between each local impedance, given by:

$$Z_{\text{cell}} = \left( \sum_{j=1}^N \frac{1}{Z_j} \right)^{-1} \quad (48)$$

where N is the number of integration steps in which the channel length has been discretized during the numerical resolution of the DMFC anode polarization model.

## 4. Modeling results discussion

### 4.1. Steady-state polarization

The increased complexity of the developed model, the more detailed description of the DMFC operation and the necessity to reproduce both steady-state polarization and impedance data make the calibration procedure more difficult than in the previous models [27,34]. However the model reproduces anode polarization

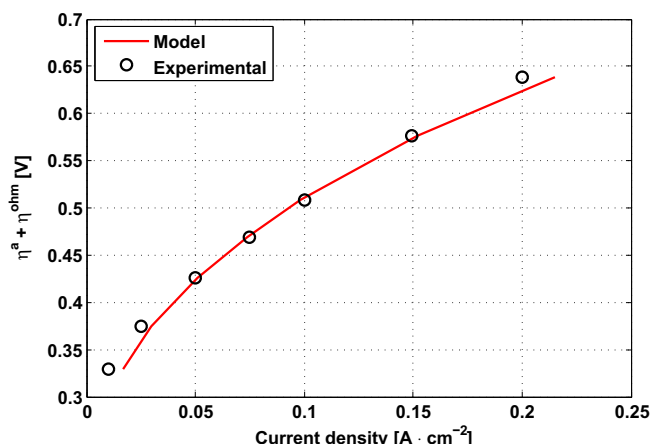


Fig. 4. Comparison of the simulated and measured anode polarization.

Table 1

Assumed and calibrated kinetic and mass transport parameters.

$D_{\text{GDL,CH}_3\text{OH}}^L$	$10^{-5.4163-999.778/T} \times 10^4$	$\text{cm}^2 \text{ s}^{-1}$	[51]
$D_{\text{GDL,CH}_3\text{OH}}^G$	$1.52 \times 10^{-2}$	$\text{cm}^2 \text{ s}^{-1}$	Calibrated
$C_{\text{ref},1}$	$1 \times 10^{-3}$	$\text{mol cm}^{-3}$	—
$C_{\text{ref},2}$	$5.5 \times 10^{-2}$	$\text{mol cm}^{-3}$	—
$\alpha_1$	0.74	—	Calibrated
$\alpha_2$	0.38	—	Calibrated
$i_{s1}$	$6.18 \times 10^{-5} \times \exp(66712/R \times (1/353 - 1/T))$	$\text{A cm}^{-3}$	Calibrated
$i_{s2}$	$2.39 \times 10^{-2} \times \exp(66712/R \times (1/353 - 1/T))$	$\text{A cm}^{-3}$	Calibrated
$\rho_{\text{H}_2\text{O}}$	$(-0.0028 \times (T - 273)^2 - 0.1757 \times (T - 273) + 1003.8) \times 10^{-3}$	$\text{g cm}^{-3}$	[51]
$\mu_{\text{H}_2\text{O}}$	$3.56 \times 10^{-4}$	$\text{Pa s}$	[51]
$\sigma_{\text{H}_2\text{O}}$	$6.25 \times 10^{-2}$	$\text{N m}^{-1}$	[51]
$\sigma_t$	$4 \times 10^{-3}$	$\Omega^{-1} \text{ cm}^{-1}$	Assumed
$K_{\text{H,CH}_3\text{OH}}$	$2.2 \times \exp(5200 \times (1/T - 1/298))$	$\text{mol J}^{-1}$	[51]
$K_{\text{GDL}}$	$1 \times 10^{-14}$	$\text{m}^2$	Assumed
$\theta_c$	130	$^\circ$	Assumed
$F$	96485	$\text{C mol}^{-1}$	—
$R$	8314	$\text{J mol}^{-1} \text{ K}^{-1}$	—
$l_{\text{GDL}}$	$3 \times 10^{-2}$	$\text{cm}$	—
$l_t$	$4 \times 10^{-3}$	$\text{cm}$	—
$A_{\text{cell}}$	22.1	$\text{cm}^2$	—
CF	0.1	—	Calibrated
$S_1$	0.75	—	Calibrated
$S_2$	2	—	Calibrated
$S_{3,0.075 \text{ A/cm}^2}$	0.085	—	Calibrated
$S_{3,0.15 \text{ A/cm}^2}$	0.13	—	Calibrated

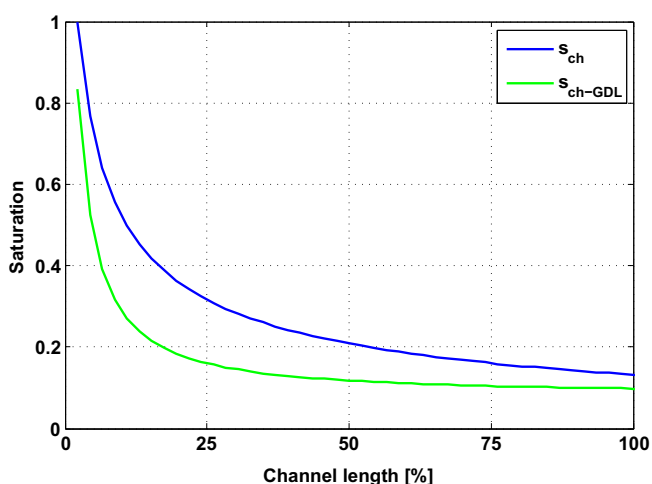


Fig. 5. Profile of  $s_{\text{ch}}$  and  $s_{\text{ch-GDL}}$  along channel length at  $0.075 \text{ A cm}^{-2}$ .

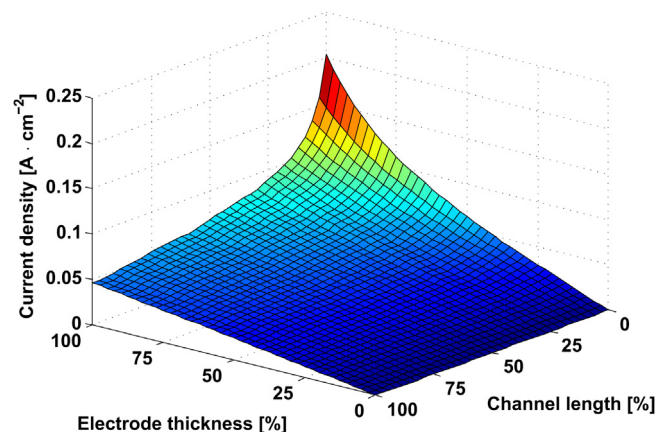


Fig. 6. Profile of current density along channel length and electrode thickness at  $0.075 \text{ A cm}^{-2}$ .

Table 2

Assumed parameters for the simulation of anode EIS.

$C_{\text{dl}}$	30	$\text{F cm}^{-3}$
$\Gamma_{\text{Pt}}$	$1 \times 10^{-3}$	$\text{mol cm}^{-3}$
$\epsilon_t$	0.12	—
$\epsilon_{\text{GDL}}$	0.6	—

with good accuracy (Fig. 4) and the assumed and calibrated parameters have reasonable values (Table 1).

The high number of calibration parameters reported in Table 1 is fundamental to simulate also the anode impedance behavior: in

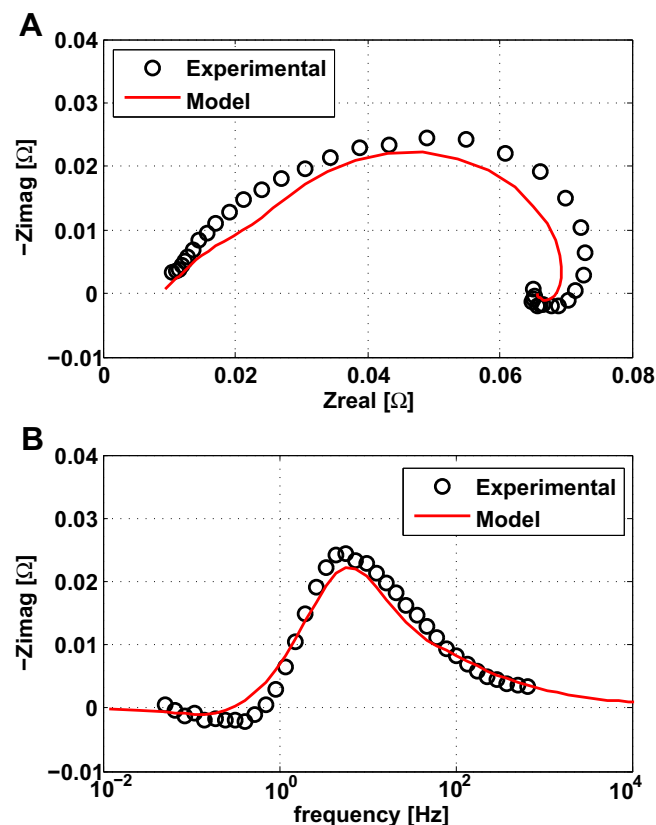


Fig. 7. Comparison of the simulated and measured impedance at  $0.075 \text{ A cm}^{-2}$ : a) Nyquist plot; b) Bode plot.

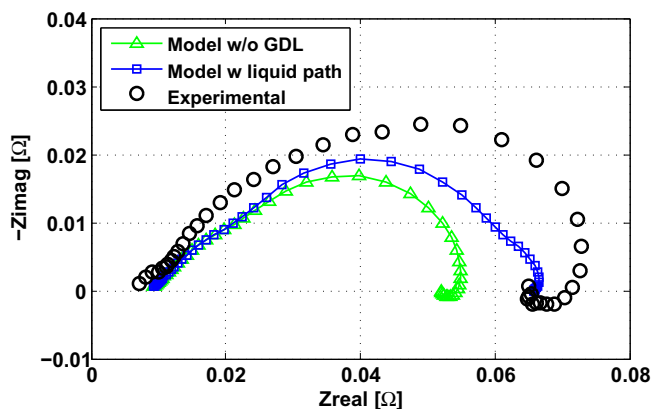


Fig. 8. Simulated anode Nyquist plot at  $0.075 \text{ A cm}^{-2}$  without the assumption of intermittent permeation and without the effect of GDL.

fact the calibration is an iterative procedure that consists in minimization of the residuals between model estimation and experimental measurements of both anode polarization and EIS. A limited number of calibration parameters would be necessary to reproduce only the polarization curve.

The resulting value of CF is lower than 1 and therefore the CL average diffusivity is lower than the diffusion layer one, coherently with reduced values of porosity and void fraction in the CL. Regarding the calibration parameters of saturation profile at channel-GDL interface, Eq. (18), the values of  $S_1$  and  $S_2$  are quite high: this implies a very strong dependence of  $s_{\text{ch-GDL}}$  on the saturation in the channel. Fig. 5 reports a comparison between the simulated profile of  $s_{\text{ch}}$  and  $s_{\text{ch-GDL}}$  along channel length: the saturation at the channel-GDL interface is lower than the channel one, coherently with the higher hydrophobicity of the diffusion media.

The resolution of the DMFC anode polarization model permits to obtain the steady-state profiles of all the physical quantities necessary for simulation of impedance behavior. By way of example Fig. 6 illustrates current density profile along channel length and electrode thickness: its value is zero at GDL interface and reaches its maximum at membrane interface.

## 4.2. Electrochemical impedance spectroscopy

### 4.2.1. Impedance simulations at $0.075 \text{ A cm}^{-2}$

All the kinetic and transport parameters necessary for the simulation of DMFC anode spectrum have been previously reported

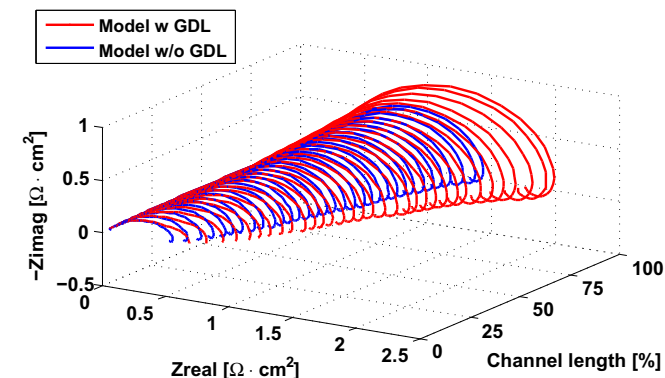


Fig. 9. Simulated anode Nyquist plot along channel length at  $0.075 \text{ A cm}^{-2}$  with and without GDL effects.

in Table 1; while the value of the double layer capacitance, active site density and porosities have been assumed, Table 2.

Fig. 7 a reports the simulated Nyquist plot at  $0.075 \text{ A cm}^{-2}$ . The model reproduces experimental observations with sufficient accuracy and it is possible to notice the presence of the linear branch due to the proton transport limitations in the CL. Moreover the detailed mass transport description of both methanol and water fluxes through the anode GDL provides an accurate estimation of the mass transport impedance and the total resistance is close to the experimental value. Fig. 7b illustrates the Bode plot: there is full agreement between model and experiment; therefore the main involved processes are correctly described.

It is very important to figure out that the developed model reproduces DMFC operating current with high accuracy: in fact the simulated value of current density, equal to  $0.074 \text{ A cm}^{-2}$ , is almost identical to the experimental one. This is a very important feature because it would be possible to obtain more accurate impedance simulations by slightly changing few physical parameters, but in this case the DMFC operating current would be rather different from the experimental one.

Fig. 8 reports impedance simulations performed with the assumption that GDL is always flooded with fully liquid pathways: the GDL liquid accumulation terms dampen the oscillations of concentrations for all the perturbation frequencies. Model predictions are inconsistent with the experimental data and this is a further confirmation that liquid convection through the GDL is an intermittent phenomenon. Furthermore Fig. 8 illustrates impedance simulations without the effect of the GDL: the concentration disturbances at the GDL-CL interface are null and the fluxes are not affected by the GDL accumulation terms. Even at low current density GDL has a relevant influence on impedance behavior.

Fig. 9 reports a comparison between model results with and without the implementation of GDL effects along channel length. It is evident that towards the end of channel the mass transport losses due to the presence of GDL are more pronounced, as expected. Moreover, also the magnitude of inductive loop increases towards the end of the channel.

Hereinafter a specific analysis is performed in order to evaluate the effects of the boundary conditions regarding the oscillating fluxes at the electrode-membrane interface. From Fig. 10 it is possible to figure out that these boundary conditions affect impedance features in the low-medium frequencies region. In particular  $\Delta N_{\text{CH}_3\text{OH}}^{\text{H}_2\text{O}}|_{\text{el-m}} = 0$  implies an increase of the total resistance and a reduction of inductive behavior, while  $\Delta N_{\text{H}_2\text{O}}^{\text{H}_2\text{O}}|_{\text{el-m}} = 0$  has the opposite effect. However all the physical phenomena are interconnected: switching off certain physical

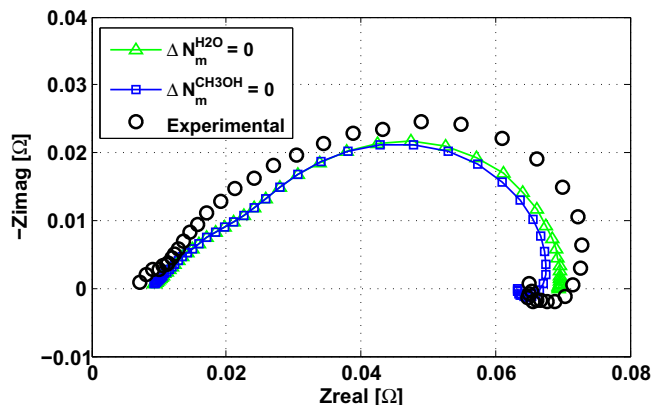


Fig. 10. Simulated anode Nyquist plot at  $0.075 \text{ A cm}^{-2}$  with  $\Delta N_{\text{CH}_3\text{OH}}^{\text{H}_2\text{O}}|_{\text{el-m}} = 0$  and  $\Delta N_{\text{H}_2\text{O}}^{\text{H}_2\text{O}}|_{\text{el-m}} = 0$ .



phenomena may affect the impedance behavior of other physical processes, therefore it is not easy to find out the origin of these different impedance features. However these effects seem to be related to a variation of both water and methanol concentrations in the CL. This is a further confirmation of the complexity of DMFC anode impedance modeling and therefore the previous model validation on three different typologies of measure at the same time, reported in Refs. [27], was fundamental to simulate impedance data with good accuracy.

#### 4.2.2. Impedance simulations at $0.15 \text{ A cm}^{-2}$

Doubling the current density the model reproduces experimental observations with sufficient accuracy, Fig. 11: the inductive behavior is no longer present and mass transport limitations seem to appear in the low frequency region. However the model slightly overestimates the total resistance.

In Fig. 11, the simulations without the effect of GDL are considerable different from the experimental observations. As expected, at high current density mass transport losses are more relevant than that at low current density, Fig. 8.

Once again the model predictions with the effects of fully liquid pathways in the GDL are inconsistent with experimental data. In this case it is possible to clearly distinguish two arches: the first one characterizes kinetic losses, while the second one is peculiar of mass transport limitations. The intermittent liquid convection does not dampen the oscillations of concentrations at GDL-CL interface for frequencies lower than 75 Hz, leading to a superimposition of the two arches. These considerations underline the difficulties in the interpretation of DMFC anode spectra: in fact mass transport limitations do not manifest themselves as a second arch, even if their contribution is relevant.

## 5. Conclusions

A physically based model of DMFC anode impedance has been developed and validated considering two different operating current values. The model includes a detailed description of water and methanol transport through diffusion layer: the former is regulated by liquid convection, that is assumed to be an intermittent phenomenon, the latter is governed by both liquid convection and gas and liquid diffusion. Moreover the CL has a finite thickness and methanol oxidation reaction involves CO adsorbed intermediate.

The developed model permits to quantify DMFC internal losses and investigate the origin of different impedance features. The main conclusions regarding DMFC anode impedance behavior are the following:

- proton transport limitations through the electrode manifest themselves as a  $45^\circ$  linear branch at high frequencies;
- the intermittent description of liquid convection through GDL entails that liquid accumulation terms dampen the oscillations of concentrations only for perturbation frequencies higher than 75 Hz. This assumption implies a superimposition between the arches peculiar of kinetic and mass transport losses and it is of fundamental importance to correctly simulate anode impedance features;
- the contribution of GDL to the impedance is relevant even at a rather low current density, such as  $0.075 \text{ A cm}^{-2}$ , and increases along channel length, as expected. Doubling the operating current density the effect of GDL is predominant and in fact without the assumption of intermittent permeation it is possible to clearly distinguish a second arch, peculiar of mass transport limitations;
- the oscillations of methanol and water fluxes through the membrane cannot be neglected, in fact they affect the shape of the spectrum in the low-medium frequency region: this increases the difficulties in the validation of the model and underlines the complexities in the interpretation of DMFC anode impedance. A specific experimental and modeling analysis of the effects of cross-over fluxes on anode impedance behavior will be carried out in future work.

## Acknowledgment

This work has been performed in the frame of the FCH-JU FP7 project Premium Act (EC Grant Agreement 256776). The authors would like to thank Prof. Dr. Wolfgang G. Bessler for the useful discussions.

## List of symbols

$C$	species concentration in the channel ( $\text{mol cm}^{-3}$ )
$\bar{C}$	time-average concentration in the channel ( $\text{mol cm}^{-3}$ )
$C_{\text{ref}}$	reference concentration ( $\text{mol cm}^{-3}$ )
$D$	diffusivity ( $\text{cm}^2 \text{s}^{-1}$ )
$\bar{D}$	time-average diffusivity ( $\text{cm}^2 \text{s}^{-1}$ )
$F$	Faraday constant ( $\text{C mol}^{-1}$ )
$R$	universal gas constant ( $\text{J mol}^{-1} \text{K}^{-1}$ )
$T$	fuel cell temperature (K)
$i$	local current density ( $\text{A cm}^{-2}$ )
$i_0$	exchange current density ( $\text{A cm}^{-3}$ )
$b$	Tafel slope (V)
$K_H$	Henry constant ( $\text{mol J}^{-1}$ )
$l$	layer thickness (cm)
$h$	channel height and width (cm)
$M$	molecular weight ( $\text{g mol}^{-1}$ )
$K$	permeability ( $\text{m}^2$ )
$N^{\text{H}_2\text{O}}$	water flux ( $\text{mol cm}^{-2} \text{s}^{-1}$ )
$N^{\text{CH}_3\text{OH}}$	methanol flux ( $\text{mol cm}^{-2} \text{s}^{-1}$ )
$p_c$	capillary pressure (Pa)
$v$	local velocity in channel ( $\text{cm s}^{-1}$ )
$x$	$x$ coordinate (cm)
$t$	time (s)
$s$	liquid saturation
$\bar{s}_{\text{GDL}}$	average liquid saturation across GDL
$CF$	correction factor
$J(s)$	Leverett function
$C_{\text{dl}}$	double layer capacitance ( $\text{F cm}^{-3}$ )

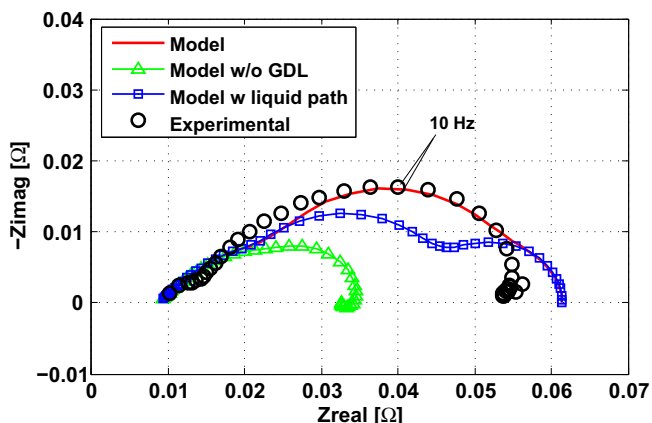


Fig. 11. Comparison of the simulated and measured Nyquist plots at  $0.15 \text{ A cm}^{-2}$ .

$Z$	impedance ( $\Omega$ or $\Omega\text{ cm}^2$ )
$V_{\text{cell}}$	cell potential difference (V)

*Greek symbol*

$\alpha$	Tafel transport coefficient
$\eta$	polarization (V)
$\sigma_{\text{H}_2\text{O}}$	surface tension ( $\text{N m}^{-1}$ )
$\rho$	compound density ( $\text{g cm}^{-3}$ )
$\mu$	compound viscosity (Pa s)
$\nu$	compound kinematic viscosity ( $\text{m}^2\text{ s}^{-1}$ )
$\theta_c$	contact angle ( $^\circ$ )
$\varepsilon$	porosity
$\omega$	angular frequency ( $\text{rad s}^{-1}$ )
$\Gamma_{\text{Pt}}$	platinum active sites density ( $\text{mol cm}^{-3}$ )
$\gamma$	surface coverage
$\sigma_{\text{t}}^{\text{GDL}}$	catalyst layer ionic conductivity ( $\Omega^{-1}\text{ cm}^{-1}$ )
$\Delta C$	average concentration difference across GDL ( $\text{mol cm}^{-3}$ )
$\Delta i$	oscillation of current density ( $\text{A cm}^{-2}$ )
$\Delta \eta$	oscillation of overpotential (V)
$\Delta C$	oscillation of concentration ( $\text{mol cm}^{-3}$ )
$\Delta N^{\text{H}_2\text{O}}$	oscillation of water flux ( $\text{mol cm}^{-2}\text{ s}^{-1}$ )
$\Delta N^{\text{CH}_3\text{OH}}$	oscillation of methanol flux ( $\text{mol cm}^{-2}\text{ s}^{-1}$ )
$\Delta \gamma$	oscillation of surface coverage
$\Delta s$	oscillation of liquid saturation

*Superscript*

$a$	relative to anode
$c$	relative to cathode
$t$	relative to catalyst layer
$G$	relative to gas phase
$L$	relative to liquid phase
GDL	relative to GDL
sat	relative to saturation
ohm	relative to ohmic
0	relative to steady-state

*Subscript*

GDL	relative to gas diffusion layer
$t$	relative to catalyst layer
$m$	relative to membrane
ch	relative to channel
el	relative to electrode
CO	relative to carbon monoxide
$\text{H}_2\text{O}$	relative to water
$\text{CH}_3\text{OH}$	relative to methanol
$\text{H}_2$	relative to hydrogen
drag	relative to electro-osmotic drag
cross	relative to cross-over
1	relative to first reaction step
2	relative to second reaction step

**References**

- [1] E. Barsoukov, J.R. Macdonald, Impedance Spectroscopy, Theory, Experiment, and Applications, second ed., Wiley-Interscience, New York, 2005.
- [2] X.Z. Yuan, C. Song, H. Wang, J.J. Zhang, Electrochemical Impedance Spectroscopy in PEM Fuel Cells, Fundamentals and Applications, Springer, London, 2010.
- [3] N.Y. Hsu, S.C. Yen, K.T. Jeng, C.C. Chien, J. Power Sources 161 (2006) 232–239.
- [4] C.Y. Du, T.S. Zhao, W.W. Yang, Electrochim. Acta 52 (2007) 5266–5271.
- [5] D. Chakraborty, I. Chorkendor, T. Johannessen, J. Power Sources 162 (2006) 1010–1022.
- [6] N. Wagner, J. Appl. Electrochem. 32 (2002) 859–863.
- [7] M.E. Orazem, B. Tribollet, Electrochemical Impedance Spectroscopy, Wiley, New York, 2008.
- [8] S.K. Roy, M.E. Orazem, B. Tribollet, J. Electrochem. Soc. 154 (2007) B1378–B1388.
- [9] C.Y. Du, T.S. Zhao, C. Xu, J. Power Sources 167 (2007) 265–271.
- [10] Y. Shi, H. Wang, N. Cai, J. Power Sources 208 (2012) 24–34.
- [11] A. Biebler, L.J. Gauckler, Solid State Ionics 146 (2002) 23–41.
- [12] Y. Shi, N. Cai, Z. Mao, Int. J. Hydrogen Energy 37 (2012) 1037–1043.
- [13] J. Deseure, J. Power Sources 178 (2008) 323–333.
- [14] M. Eikerling, A.A. Kornyshev, J. Electroanal. Chem. 475 (1999) 107–123.
- [15] W.G. Bessler, Solid State Ionics 176 (2005) 997–1011.
- [16] W.G. Bessler, S. Gewies, M. Vogler, Electrochim. Acta 53 (2007) 1782–1800.
- [17] S. Gewies, W.G. Bessler, J. Electrochem. Soc. 155 (2008) B937–B952.
- [18] T.E. Springer, T.A. Zawodzinski, M.S. Wilson, S. Gottesfeld, J. Electrochem. Soc. 143 (1996) 587–599.
- [19] Q. Guo, R.E. White, J. Electrochem. Soc. 151 (2004) E133–E149.
- [20] A.A. Kulikovskiy, J. Electroanal. Chem. 669 (2012) 28–34.
- [21] A.A. Kulikovskiy, Electrochem. Commun. 24 (2012) 65–68.
- [22] M. Chen, C.Y. Du, G.P. Yin, P.F. Shi, T.S. Zhao, Int. J. Hydrogen Energy 34 (2009) 1522–1530.
- [23] U. Krewer, M. Christov, T. Vidakovic, K. Sundmacher, J. Electroanal. Chem. 589 (2006) 148–159.
- [24] B. Bensmann, M. Petkovska, T. Vidaković-Koch, R. Hanke-Rauschenbach, K. Sundmacher, J. Electrochem. Soc. 157 (2010) B1279–B1289.
- [25] A. Casalegno, R. Marchesi, J. Power Sources 175 (2008) 372–382.
- [26] A. Casalegno, R. Marchesi, J. Power Sources 185 (2008) 318–330.
- [27] M. Zago, A. Casalegno, C. Santoro, R. Marchesi, J. Power Sources 217 (2012) 381–391.
- [28] J.T. Mueller, P.M. Urban, J. Power Sources 75 (1998) 139–143.
- [29] J.T. Müller, P.M. Urban, W.F. Hölderich, J. Power Sources 84 (1999) 157–160.
- [30] J.P. Diard, N. Glandut, P. Landaud, B.L. Gorrec, C. Montella, Electrochim. Acta 48 (2003) 555–562.
- [31] X. Wang, J.M. Hu, I.M. Hsing, J. Electroanal. Chem. 562 (2004) 73–80.
- [32] S.K. Roy, M.E. Orazem, J. Electrochem. Soc. 154 (2007) B883–B891.
- [33] S.H. Yang, C.Y. Chen, W.J. Wang, J. Power Sources 195 (2010) 3536–3545.
- [34] A. Casalegno, R. Marchesi, D. Parenti, Fuel Cells 8 (2008) 37–44.
- [35] U. Pasaogullari, C.Y. Wang, J. Electrochem. Soc. 151 (2004) A399–A406.
- [36] U. Pasaogullari, C.Y. Wang, Electrochim. Acta 49 (2004) 4359–4369.
- [37] S. Litster, D. Sinton, N. Djilali, J. Power Sources 154 (2006) 95–105.
- [38] T.L. Liu, C. Pan, J. Power Sources 207 (2012) 60–69.
- [39] X. Zhu, P.C. Sui, N. Djilali, J. Power Sources 181 (2008) 101–115.
- [40] Y. Ding, H.T. Bi, D.P. Wilkinson, J. Power Sources 195 (2010) 7278–7288.
- [41] P. Piela, R. Fields, P. Zelenay, J. Electrochem. Soc. 153 (2006) A1902–A1913.
- [42] C.M. Lai, J.C. Lin, K.L. Hsueh, C.P. Hwang, et al., Int. J. Hydrogen Energy 32 (2007) 4381–4388.
- [43] T.S. Zhao, C. Xu, R. Chen, W.W. Yang, Prog. Energy Combust. Sci. 35 (2009) 275–292.
- [44] Y.J. Kim, W.H. Hong, S.I. Woo, H.K. Lee, J. Power Sources 159 (2006) 491–500.
- [45] H. Dohle, J. Divisek, J. Mergel, H.F. Oetjen, et al., J. Power Sources 105 (2002) 274–282.
- [46] C.E. Shaffer, C.Y. Wang, Electrochim. Acta 54 (2009) 5761–5769.
- [47] F. Liu, C.Y. Wang, Electrochim. Acta 53 (2008) 5517–5522.
- [48] W.W. Yang, T.S. Zhao, Electrochim. Acta 52 (2007) 6125–6140.
- [49] Z.H. Wang, C.Y. Wang, J. Electrochem. Soc. 150 (2003) A508–A519.
- [50] X. Wang, T.V. Nguyen, J. Electrochem. Soc. 157 (2010) B496–B505.
- [51] NIST Standard Reference Database 106, IUPAC–NIST Solubility Database, 2003.